PROCEEDINGS A

royalsocietypublishing.org/journal/rspa

Research

Cite this article: Burson-Thomas CB, Harvey TJ, Fletcher L, Wellman R, Pierron F, Wood RJK. 2023 Investigating high-speed liquid impingement with full-field measurements. *Proc. R. Soc. A* **479**: 20230023. https://doi.org/10.1098/rspa.2023.0023

Received: 10 January 2023
Accepted: 25 August 2023

Subject Areas:
mechanical engineering

Keywords:
liquid impingement, full-field measurements, water droplet erosion, ultra-high-speed imaging, grid method

Author for correspondence:
C. B. Burson-Thomas
e-mail: c.b.burson-thomas@soton.ac.uk

Investigating high-speed liquid impingement with full-field measurements

C. B. Burson-Thomas[1], T. J. Harvey[1], L. Fletcher[1], R. Wellman[2], F. Pierron[1] and R. J. K. Wood[1]

[1]Mechanical Engineering, School of Engineering, University of Southampton, Southampton, SO17 1BJ, UK
[2]Surface Engineering, Rolls-Royce plc., Derby, DE24 8BJ, UK

CBB-T, 0000-0001-9308-4669

Repeated high-speed liquid impingement on solid surfaces results in erosion that can have undesirable consequences. In recent years, the capacity of model predictions has exceeded the experimental measurements of an impingement; this work closes the gap. Using the grid method, tens of thousands of individual measurements of surface displacement were taken of the response of a polymethylmethacrylate test specimen to the impingement of a high-speed ($233\,\mathrm{m\,s^{-1}}$) curved-fronted water jet. The full-field measurements were taken at a rate of 5 MHz and interpreted using two models based on differing sets of assumptions. The results support the current qualitative description of a high-speed impingement. However, the widespread assumption of a rigid solid surface in existing analysis and modelling was found to be inaccurate: only the model that recognized the effect of the compliance of the solid surface was successful in predicting the measured temporal and spatial variation in displacement and acceleration. This model predicted that the energy absorbed by the solid surface was less than 0.3% of the total kinetic energy of the equivalent droplet impingement.

1. Introduction

The erosion of engineering components by the repeated impingement of high-speed ($50\,\mathrm{m\,s^{-1}}$ and above [1]) droplets of water is a challenge to the efficient

THE ROYAL SOCIETY PUBLISHING

running and function of steam turbine blades [2], leading surfaces of high-speed aircraft [3], pipes carrying wet steam in nuclear power plants [4], wind turbine blades [5], compressor blades [6] and aeroengine fan blades [7]. Following nearly a century of research activity [8], the complexities of this form of erosive wear have meant a theory of water droplet erosion (WDE) established from first principles has continued to elude the research community. To advance fundamental understanding, researchers have frequently focused on an individual high-speed droplet impingement, in both modelling and experiment [9]. By deconstructing the material and surface evolution, which occurs over thousands of impingements, to focus on an individual event, it has been possible to understand in greater detail how changes in relevant parameters effect the dynamic mechanical loading that drives the erosion—particularly in the early stages. This has high industrial relevance when alternative component design strategies to minimize the effect of the dynamic loading are explored.

Repeated high-speed droplet impingement leads to erosion due to the compressible behaviour of the liquid in the very early stages of contact [10]. This results in a two-stage process of impingement: the droplet initially behaves in a manner one might expect more from a solid than a liquid, before flowing along the surface [11,12]. This is described and explained later, as well as being shown in figure 1. The quantitative information provided has been calculated for typical velocities of interest, 150–400 m s^{-1}, and typical droplet diameters, 2 mm or less.

(i) *Initial 'compressible' stage.* The initial compressible behaviour is caused by the finite rate at which displacement propagates through the liquid—the speed of the shock front. For water droplets, the shock speed is often approximated as a linear function of impingement velocity [14] and has a magnitude of approximately 2000 m s^{-1}. However, in the very early stages of the impingement, the boundary between the surfaces of the droplet and solid material—the 'contact periphery' (annotated on figure 1*a*)—is moving faster. Thus, the shock front cannot extend beyond the contact periphery and is attached to this boundary. This results in a region of liquid, trapped behind the shock front and solid surface, being forced to occupy a smaller volume than previously. The liquid resists this compression and applies high pressure on the solid surface in response. The Bernoulli stagnation pressure, which predicts the magnitude if a continuous stream of liquid were to impinge at this velocity, is at least an order of magnitude lower. The 'water-hammer' pressure [8] is frequently used to estimate the pressure during the compressible stage and is of the order of hundreds of MPa.

(ii) *Secondary 'flow' stage.* Less than a microsecond after the start of the impingement, the shock front overtakes the contact periphery, due to the continued reduction in the rate of the contact periphery's expansion. This means the compressed liquid now has access to the free surface of the droplet, and two events occur: high-velocity flows of liquid in a radial direction are ejected (shown in figure 1*b*), and release waves propagate from the contact periphery to the central axis, reducing the pressure magnitude on the solid surface to the much lower value predicted by the Bernoulli stagnation pressure. The velocity of the lateral jets are significantly higher than the impingement velocity, typically two to three times [15] the impingement velocity—although some measurements have been up to ten times greater [16].

For an initially smooth solid surface, it is the effect of the dynamic loading (high pressure applied during the short compressible stage and then rapidly removed at the beginning of the flow stage), which leads to the first material damage, which initiates the process of erosion. Lateral outflow jetting only starts contributing to the process of material removal once a surface discontinuity or pit has become established [17]. Many engineering components that suffer from WDE in-service start their life with surfaces that are smooth (well machined/finished). Frequently, the industrial challenge is how to maintain the initially smooth surface condition for as long as possible,

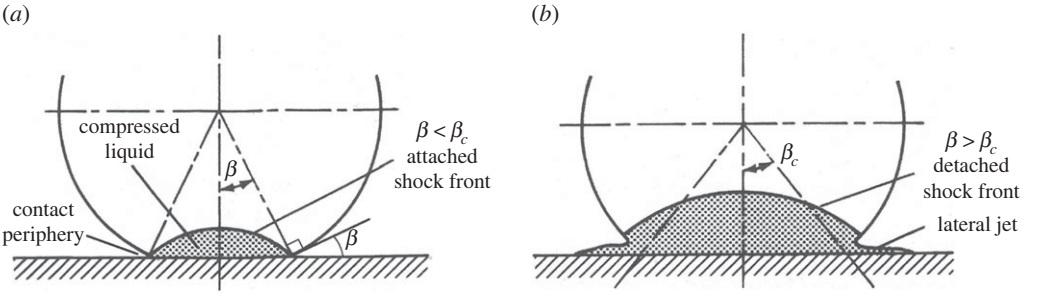

Figure 1. Two main stages of a high-speed droplet impingement: compressible and flow (adapted from [12]). The transition between these stages occurs at some critical angle subtended by the contact periphery (as it moves across the surface of the solid) from the droplet centre (β_c). (*a*) Initial 'compressible' stage, the compressed liquid generates the high 'water-hammer' pressure on the solid surface. (*b*) Secondary 'flow' stage, lateral outflow jetting interacts with discontinuities or pits on surface to contribute to water droplet erosion [13].

enabling greater retention of as-manufactured performance characteristics and increasing service-life [18]. Thus, the dynamic loading and its effect on the solid are of significant interest. In response, researchers have frequently focused on this in both fundamental experimental and modelling studies.

Table 1 describes approaches taken in previous fundamental experimental work. These studies have led to a number of significant developments in understanding: demonstrating that the applied pressure is indeed non-uniform [19], as theoretical predictions had suggested [24], as well as showing that jetting occurs later [21] than suggested by rigid theory [10]. However, when more recent modelling efforts are contrasted with the available experimental results for comparison, a fidelity gap is clear: models are able to predict the temporal and spatial response of thousands of individual points, whereas the quantitative experimental measurements consist of either the temporal response of one point in space or a spatially varying maximum value. Some modelling studies have used schlieren images to validate their predictions [25,26]. Yet, despite their many qualities, the schlieren images are primarily qualitative in nature. There remains significant uncertainty surrounding the exact nature of the dynamic loading resulting from a high-speed liquid impingement; there has not been sufficiently precise and detailed experimental measurements available to fully assess the accuracy of the models. What is required are experimental measurements as insightful as the schlieren images but quantitative in nature: where the deformation, due to the propagation of the stress wave, is not just visualized but measured.

In this work, we have sought to address this need by taking tens of thousands of measurements of displacement every 200 ns. A test specimen manufactured from polymethylmethacrylate (PMMA) was subjected to a high-speed impingement of water to record its full-field response. PMMA was selected due to its relatively low modulus (greater displacements for a given load) and comparatively well-understood response to high-speed liquid impingement [27]. This is described in the next section. To better interpret the experimental results, two models were created. Both used predictions of an analytical loading function as an input to a explicit finite element (FE) simulation; however, one model assumed the surface was rigid and the other adjusted for compliance of the solid surface. The detail of how these models were constructed follows the section on the experimental methodology. Subsequent to this, the results are presented and discussed, and finally, conclusions are offered. While the results, discussion and conclusions will be primarily of interest to those investigating WDE, it is expected that there will be significant interest from those developing models that incorporate the compressible behaviour of liquids—it is a rich experimental data set against which to validate.

Table 1. Experimental methodologies employed to investigate fundamental understanding.

approach	description	nature of measurement(s)
piezo-electric transducers	signals from suitably mounted piezo-electric transducers have been used by a number of researchers [15,19,20] to characterize the pressure applied	both spatial distributions of local maximum [19] and temporal variations in pressure at an individual location [15,20] have been measured
schlieren imaging	during the 1980s and 1990s, the research group based at the Cavendish Laboratory (Cambridge, UK) conducted extensive research using high-speed photography with schlieren optics [15,16,21,22]. This technique enabled the propagation of stress waves in the solid, and shock waves in the impinging liquid, to be visualized	the propagation and interaction of waves in 'two-dimensional' drops and wedges [16,21,22], as well as axisymmetric impingements [15], were visualized with inter-frame times equal to and less than 1 µs
photon Doppler velocimetry (PDV)	Hong & Moon [23] used PDV to measure the maximum velocity of the rear of an impinged plate, which can be used to calculate the maximum pressure exerted on the top surface	maximum impingement pressures, for different impingement velocities, were calculated from measured specimen response

2. Experimental methodology

Thanks to the progress of digital cameras and image processing algorithms, full-field measurements of deformation have spread widely within the experimental mechanics community in the last decade. They provide a large number of data points (typically thousands), hence the denomination 'full-field', though spatially dense might be more appropriate as the data are still discrete. There are several different full-field approaches to measure the response of a material experiencing dynamic deformation [28]. The grid method was selected due to the good compromise it offers between measurement resolution and spatial resolution [29]. However, before any displacement field can be measured, a high-speed liquid impingement is required to generate the correct dynamic loading. This was created by a rig at the University of Southampton, results from which have recently been published [13], based on a methodology that has been offering insights for over five decades [30]. For a more detailed account of the construction and characterization of the rig, readers are advised to consult Burson-Thomas *et al.* [13]. The key points are summarized below, along with the adaptations made for full-field imaging.

(a) Generating a high-speed liquid impingement

The rig generates a high-speed curved-fronted water jet to create the appropriate dynamic loading. This is an experimental analogue of a high-speed droplet impingement and enables the test specimen to be kept stationary. Other studies [16] have used a stationary droplet and moving test specimen to generate the high-speed impingement. It is not possible to accelerate a spherical droplet to the required velocity; it transforms to mist before the necessary velocity can be reached [9,31]. If the jet front forms a perfect spherical cap, sufficiently large that jetting occurs in advance of the contact periphery reaching the cap edge, and then the compressible stage should be identical to that produced by a droplet of the same radius and impingement velocity [32]. However, as has been observed by previous researchers [25,32,33], although the jet front is indeed curved, it does not form a perfect spherical cap before it impinges the specimen. In our previous work [13], high-speed digital imaging and an edge-detection algorithm [34] were used to track

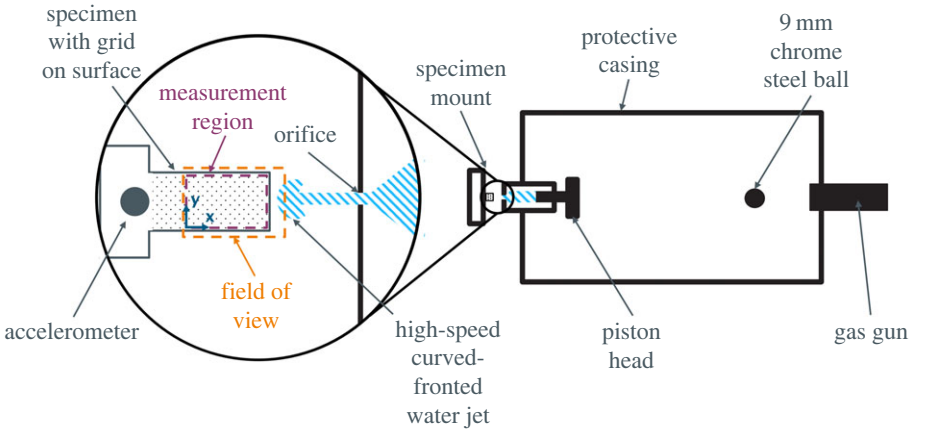

Figure 2. Schematic of the experimental set up.

Table 2. Key experimental parameters selected to produce consistent high-speed curved-fronted jets.

parameter	value
stand-off distance	10 mm (uncertainty $\pm$ 1 mm)
water	tap water
surface preparation	as cut (with diamond cut-off wheel)
gas gun pressure	140 kPa
orifice diameter	0.6 mm
ball velocity at barrel exit	55 m s^{-1} (mean value)

the form of the jet front. If assumed to be axisymmetric, a second-order polynomial was found to be more accurate description of the form (which, when rotated around its axis of symmetry describes the shape of the jet front). By employing the fundamental assumptions and approach of 'Guided Acoustic Shock', as explained in the study by Lesser [1] and using the conservation of impulse, a relationship between the polynomial describing the jet front and an 'equivalent' droplet radius was derived [13]:

$$r \approx \frac{1}{2a}. \tag{2.1}$$

This equation shows the conversion between the coefficient of the second-order term (a), in the polynomial describing the jet front ($f(x) = ax^2$), and droplet radius (r) that would impart the same impulse should the impingement velocity be consistent. Note that a geometric interpretation of this equation is also available: equation (2.1) approximates r to be the radius of curvature of the parabolic jet front at its tip.

Figure 2 shows the experimental set up. To create a high-speed curved-fronted jet, the piston and nozzle assembly are filled with water and placed on a mount within the protective casing. A 9 mm chrome steel ball is loaded into the barrel of the gas gun, and the door of the protective casing closed. The gun is then fired, and the accelerated ball impacts the piston head. This impact results in a high-speed jet emerging from the orifice, where air ablation causes the front to become curved as the jet crosses the stand-off distance. The pressure of the gas gun, orifice diameter, distance between orifice and the specimen (stand-off) and other relevant parameters were consistent with our previous study [13]. These are summarized in table 2.

Mean values of equivalent radius and velocity from the previous characterization of the jets [13] are assumed as identical experimental parameters were employed. The mean

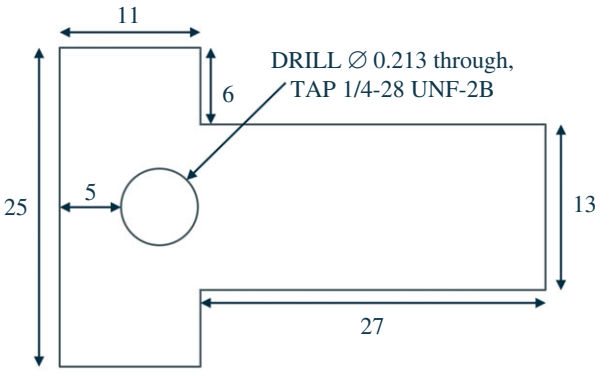

Figure 3. Profile of test specimen, where out-of-plane thickness is 3 mm. Tapped hole is for mounting of accelerometer. All dimensions are given in millimetres, except tapped hole dimensions, which are in inches.

impingement velocity is 233 m s^{-1} and standard deviation is 11.8 m s^{-1}. The mean equivalent radius (determined using equation (2.1)) is 2.4 mm and standard deviation is 0.44 mm. These have been calculated from over 30 individual measurements, in the 1 mm before the jet impinges the test specimen.

(b) Test specimen and full-field measurement

To use the grid method to make full-field measurements of in-plane displacement, regular markings (the 'grid') must be made on the surface under investigation [29]. One side of a flat sheet of PMMA (supplied by theplasticshop.com [35]) was spray painted with a thin layer of white rubber-based paint. Once dry, a regular grid with an average 'pitch' (spatial period) of 0.337 mm was printed on the painted surface using a flat-bed printer, which was the finest pitch that could be reliably produced using the printing equipment available. This procedure for creating the grid avoids defects from trapped air when, instead, a separately manufactured grid is bonded to the specimen surface [36,37]. Finally, the test specimen was cut out (using a diamond cut-off wheel) from this 3-mm-thick sheet. The thickness was selected to maximize displacements on the surface, while not being so thin as to affect the impingement of the high-speed water. Figure 3 shows the dimensions of the final PMMA specimen. The shape was created to enable the two lateral free edges (in addition to the edge impinged) to be in the camera field of view, while maintaining a wider region at the non-impingement end for easier clamping in the specimen mount. The surface to be impinged was not perfectly perpendicular to motion of the jet (observable in figure 4): a small deviation of 1.5° from a perfectly perpendicular impingement was measured on the image. However, previous studies investigating the effect of oblique angles of incidence on high-speed liquid impingement [20,32] conclude that this deviation is too small to make any significant difference to the dynamic loading created. It is therefore assumed that the impingement can be considered perpendicular.

Figure 4 shows an individual frame from one of the ultra-high-speed (5 MHz) recordings made, before the jet impinging the specimen. First, a region must be selected on the original image that is to be processed (rectangular area containing only grid), the 'region of interest', as shown in figure 4. The smaller enlarged region in figure 4 shows the measurements of light intensity at each pixel, recorded by the camera detector. The grid method is able to translate these measurements of light intensity into a measurement of displacement at each pixel. Displacements are obtained from the phase difference between the reference (undeformed) and deformed images. This phase difference is computed using a windowed discrete Fourier transform with a triangular weighting function (suitable for localized phenomena and low noise [29]). The Fourier transform required points one grid pitch either side of the spatial point in question to determine the local phase value.

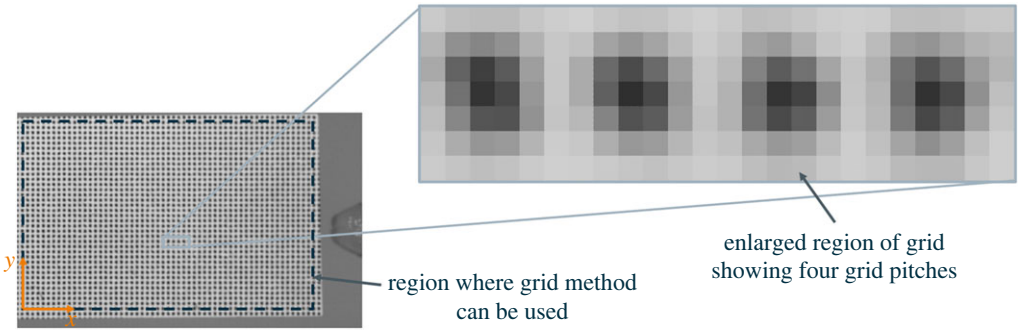

Figure 4. Example image taken using the ultra-high-speed camera with region of interest highlighted. A border of one grid pitch is required for accurate processing. The coordinate system is also defined, with the origin in the bottom-left corner of the region of interest. A smaller region has been enlarged to show the individual measurements of light intensity at each pixel.

Therefore, one grid pitch existed between the perimeter of the region of interest and the specimen edge (as shown in figure 4). It should be noted that the iterative version of the algorithm is used to compensate for any small defects in the grid ('Procedure 2' in Grédiac *et al.* [29]). The open-source Matlab code, which accompanies the review by Grédiac *et al.* [29], was used to process the grey-level images from the camera. Further details can be found in the study by Grédiac *et al.* [29]. This results in a measurement of displacement, in both x and y directions, at each pixel[1] in the selected region, for each frame of the ultra-high-speed recording. Given that the detector on the ultra-high-speed camera (Shimadzu HPV-X) is 400 by 250 pixels, and the selected region fills the majority of the image, tens of thousands of individual measurements of displacement (in both x and y directions) are extracted from just one image. The camera was used at its fastest speed, 5 MHz. Thus, the extraction of tens of thousands of displacement measurements occurred every 200 ns.

The design of the detector on the Shimadzu HPV-X, specifically the low pixel fill-factor, means that improved results are obtained by a slight defocusing ('blurring') of the image. Fletcher *et al.* [37,38] devised a protocol for setting the appropriate level of blur; this was used before the experimental runs. The camera records a maximum of 128 images, which, given the frame-rate, results in 25.6 µs of total recording time. While the triggering system previously developed [13] was sufficiently accurate for the pre-triggering of the flash (rise time of approximately 100 µs), it was not sufficiently accurate for the camera triggering. An accelerometer was mounted at the non-impingement end of the specimen and connected to the external trigger on the camera via an amplifier. The camera was post-triggered based on the accelerometer signal. This proved to be a very repeatable methodology, with almost all runs being completely synchronized (impingement occurring at exactly the same frame number). The frame number where the impingement commenced was determined by visual inspection of the geometry of the impinging jet (in the image stack). Table 3 summarizes the key parameters used for ultra-high-speed imaging and the grid method. Also included in table 3 are the displacement and acceleration resolutions for the full-field measurement. The displacement resolution is defined as the standard deviation of the spatial map, using stationary images (prior to loading). The bias 'mean' was much lower and negligible. The acceleration resolution is the standard deviation of the spatial map (of acceleration) calculated from displacements, using centred finite-difference numerical differentiation.

[1]Though the measurements at each pixel are not independent.

Table 3. Key parameters for ultra-high-speed imaging and the grid method.

parameter	value
camera	Shimadzu HPV-X
lens	Sigma 105 mm
stand-off distance	20 cm
flash	Bowens Gemini 1000 Pro (1 ms pulse width)
accelerometer for camera trigger	Dytran 3019A
accelerometer amplifier	Dytran 4105C (gain set to 'X100')
pixel array size	400 by 250 (22.5 mm by 14 mm)
total number of frames	128
inter-frame time	200 ns
integration (exposure) time	110 ns
grid pitch (p)	0.337 mm
grid sampling	6 pixels/period
window for Fourier transform	Bi-triangular
width of Fourier transform window	Two grid pitches
field of view	22.47 mm by 14.04 mm
displacement resolution[a]	0.4 mm, 0.008 pixel, $p/800$
acceleration resolution[b]	4.6×10^6 m s^{-2}

[a]Obtained from a set of stationary images prior to loading.

[b]Calculated from displacements using centred finite-difference numerical differentiation.

3. Modelling and data processing

There has been a wide variety of models and modelling approaches explored for high-speed liquid impingement. A key dividing line between the existing models is whether the method assumes the solid surface is rigid or compliant. Models that assume a rigid solid surface continue to be developed [39], despite having been strong experimental evidence for decades that the compliance of the solid surface significantly affects the high-speed impingement [16]. To investigate the importance of solid compliance further, two models of the experimental test were constructed: one assuming the solid surface is rigid and another that incorporated solid compliance.

The modelling methodology was inspired by the approach developed by deBotton [40,41], who used the established analytical theory [11] to define the loading in an explicit FE simulation of the solid response. The specific implementation here is different, but the overarching concept is the same: analytical models are used to define the load imparted by the droplet impingement and explicit FE used to simulate the dynamic response of the solid.

(a) Analytical models of dynamic loading

The loading model is driven by two parameters: the pressure exerted on the surface and the area over which it acts. Though both modelling [24,42,43] and experiment [19] showed that a non-uniform pressure develops on the surface, the relatively short duration of significant non-uniformity means that the pressure has frequently been assumed to be spatially uniform [11,41,44]. This is also the case here. In the remainder of this section, the equations used to represent the pressure magnitude and temporal variation in area will be described for each

model. The temporal evolution of area is subdivided into two periods: (1) when the area is expanding, until release waves propagate from the contact periphery towards the central axis and (2) when the area is contracting, until the release waves have reached the central axis. As the droplet impingement is assumed to be axisymmetric (sphere impinging a planar surface), the expanding and contracting area will be circular, where the temporal variation in radius is the model parameter.

(i) Rigid model

When the solid surface is assumed rigid, the pressure magnitude (p) is provided by the 'water-hammer' equation [8],

$$p = \rho_1 C_1 V, \tag{3.1}$$

where ρ_1 is the density of the liquid and V is the impingement velocity (perpendicular to the surface). The shock speed within the liquid droplet, C_1, is approximated by a linear function of the impingement velocity [14]:

$$C_1 = C_0 + kV. \tag{3.2}$$

For water, the acoustic velocity, C_0, is approximately $1500\,\mathrm{m\,s^{-1}}$, and k (a constant) is approximately 2 [14].

The temporal variation in the radius of the circular area, while it is expanding, ($X_e(t)$) can be approximated [44,45] as follows:

$$X_e(t) \approx (2rVt)^{1/2}, \tag{3.3}$$

which is a function of three variables: droplet radius (r), impingement velocity (V) and time (t). The expansion continues until the shock front is able to overtake the contact periphery. This happens when the velocity of the contact periphery, in the direction tangential to the droplet surface, reduces to C_1 [10] (figure 5). The radial position where this occurs (X_c) is given by

$$X_c = \frac{Vr}{C_1}. \tag{3.4}$$

The time when the contact periphery reaches this radial position (t_c) can be approximated by

$$t_c \approx \frac{rV}{2C_1^2}. \tag{3.5}$$

From this point, the radius of the circular area (over which the pressure is applied) is no longer controlled by the contact periphery. The head of the release waves, which are emitted from the contact periphery towards the central axis, dictates the area dimensions. During this contraction of the area (when $t > t_c$), the temporal variation in the radius ($X_r(t)$) is provided by

$$X_r(t) = X_c - C_1(t - t_c). \tag{3.6}$$

The time when the release waves reach the central axis (t_r), and the high-pressure loading generated by the compressible behaviour of the water has finished, is approximated by

$$t_r \approx \frac{3rV}{2C_1^2}. \tag{3.7}$$

(ii) Compliant model

To include the effect of surface compliance into the calculation of the pressure magnitude, the motion of the solid at the surface is considered. The change in the velocity of the liquid, which is assumed to be equal to the impingement velocity in the water-hammer equation (equation 3.1), is instead the difference between the impingement velocity (V) and the motion of the solid surface

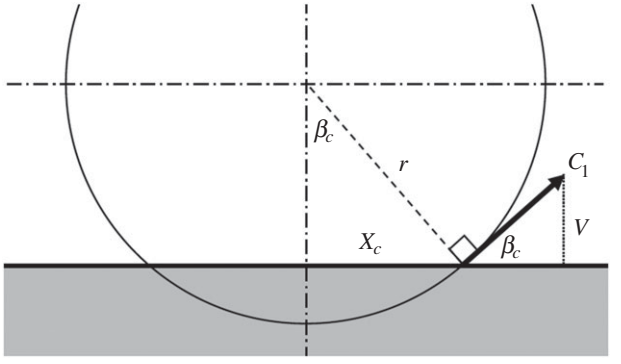

Figure 5. When the velocity of the contact periphery, in the direction tangential to the surface of the droplet, reduces to the shock speed (C_1), the shock front is able to overtake the contact periphery [10].

as a response to the loading [14]. The resulting equation for pressure, commonly attributed [17] to de Haller [46], can be expressed as follows:

$$p = \frac{\rho_1 C_1 V}{1 + \rho_1 C_1 / \rho_2 C_2}. \tag{3.8}$$

The effect of solid surface compliance is captured by the addition of the density of the solid, ρ_2, and compression wave speed in the solid, C_2. This wave speed (C_2) is $\sqrt{E/\rho_2}$, where E is the Young's modulus of the solid.

It has been shown that, as the compliance of the surface increases, the point at which lateral outflow jetting occurs is increasingly delayed [16]. The angle subtended by the contact periphery (as it moves across the surface of the solid) from the droplet centre, β (figure 1), is used to quantify the delay. Field *et al.* [16] measured the value of β when jetting occurred (β_j) for different sized droplet impingements on PMMA. Although some small variation was present, the mean value of 14° offers a good estimate of the point at which jetting will occur on this material. To calculate the position of the contact periphery when jetting occurs (X_j), the trigonometric relationship

$$X_j = r \sin \beta_j \tag{3.9}$$

was used. The time at which this occurs (t_j) is given by

$$t_j = \frac{r \sin^2 \beta_j}{2V}, \tag{3.10}$$

which is formed by setting equations (3.3) and (3.9) equal to each other and rearranging. Equation (3.3) remains a valid description for the temporal variation in the radius of the circular area while it is expanding. However, the radius in the compliant model extends further to that predicted by equation (3.9) (X_j), as opposed to the prediction of equation (3.4) (X_c). Similarly, the temporal variation in the radius of the circular area, when contracting, is also predicted by the same relationship as for the rigid model, equation (3.6). However, for the compliant model, the value of X_c is replaced by X_j, and the value of t_c is exchanged for t_j.

(b) Numerical model of solid response

To model the response of the experimental test specimen, a numerical simulation was implemented in Abaqus/Explicit (v6.14). The material simulated, PMMA, was assumed to be linear-elastic, homogeneous and isotropic. Table 4 shows the key simulation parameters for the numerical model. The geometry was selected to simulate only the region of the test specimen in the camera field of view, and all edges were unconstrained. The value of elastic modulus is almost double that measured by quasi-static tensile tests; the stiffness of PMMA shows significant

Table 4. Key parameters for the explicit FE simulation of the experimental test.

parameter	value
explicit FE package	Abaqus/Explicit (v6.14)
geometry	20 mm by 13 mm by 3 mm
element size	0.1 mm
element type	C3D8R[a]
nominal time step	0.02 µs ($\approx 0.5 t_{crit}$)
beta damping	0.1×10^{-7} s
density	1190 kg m^{-3} [35]
elastic modulus	5.5 GPa [47]
Poisson's ratio	0.38 [35]
impingement velocity	233 m s^{-1}
droplet radius	2.4 mm

[a]Linear quadrilateral element, with reduced integration.

sensitivity to the strain rate [48], and so an adjusted value is necessary for dynamic loading—such as that imparted by high-speed liquid impingement. The value used, 5.5 Gpa, is consistent with measurements at similar strain rates $\sim 1000\,\mathrm{s}^{-1}$ [47]. The impingement velocity and droplet radius are mean values from previous characterization of the high-speed jets [13], where the same experimental settings were used.

To input the loading from each analytical model to the explicit FE software, several loading steps were created. These approximated the dynamic loading on the surface, such that the total impulse was conserved. This is shown in figure 6, where the temporal variation in force predicted by each model is compared with the approximation made. To create the loading steps efficiently and accurately, a Python script was written that defined the simulation and relevant parameters. There were four main steps in this workflow:

(i) Create three-dimensional geometry, assign material properties, partition loaded surface to create many selectable individual surface regions to simulate the expanding contact radius, and mesh geometry with quadrilateral elements.
(ii) Define all available loading steps (determined by geometry of mesh). For each loading step, calculate at what time to shift to the next step—a higher loading when the area is expanding, lower when contracting.
(iii) Use these calculations to apply multiple load steps, selecting the appropriate individual surface regions and apply a uniform pressure equal to the value from the relevant analytical model, using amplitudes to activate and deactivate the load step at the appropriate point in time.
(iv) Finally, run the simulation for the appropriate duration and export key data.

Finally, the numerical model was verified by inferring the applied force from the FE data and by checking whether it was consistent with the analytical model. The applied force was calculated from the product of the mean acceleration of the all the nodes in the x-direction (at each temporal position) and multiplying by the mass of the modelled geometry [49].

(c) Data processing

Centred finite-difference numerical differentiation (Matlab's 'gradient' function) was used to calculate corresponding fields of acceleration in both x and y directions from the measured displacement fields.

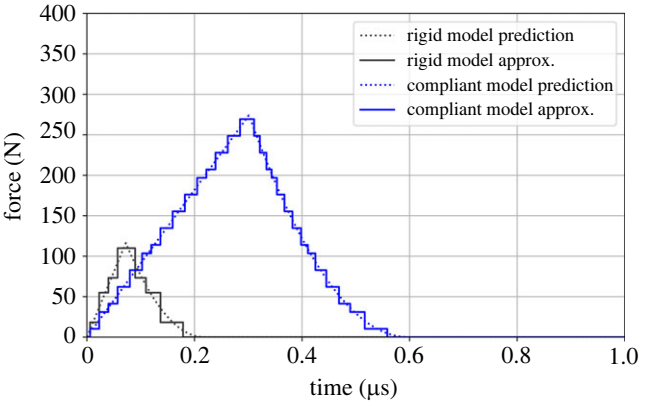

Figure 6. Approximation of temporal variation in force by creation of individual loading steps in explicit FE simulation. Both the rigid and compliant models are shown. The variation in force is generated solely by the changing area of application; the pressure remains constant—458 MPa for the rigid model (equation (3.1)) and 259 MPa for the compliant (equation (3.8)). The greater force in the compliant model is due to the larger areas over which the pressure is applied.

To compare the experimental measurements with the predictions from modelling, image deformation simulations [50] were performed. The reason for this is that FE results and experimental data are not directly comparable. Indeed, experimental results contain not only random noise but also a systematic error arising from the limited spatial resolution of the sensor. The image deformation simulations add the random and systematic errors to the modelling outputs. It was shown in the study by Lava *et al.* [51] that this was necessary to allow for accurate model validation as otherwise, false negatives and positives could easily arise. Figure 7 shows the main steps in the process. The FE displacement fields were exported and used to generate a series of synthetic greyscale images of grids encoding these displacements. The code to perform this step is open source and accompanies the study by Fletcher *et al.* [37]. The synthetic images had the same level of contrast and mean light intensity as the experimental images. They also had the same grid pitch as the real ones used in the experiment. Following this, both experimental and modelling greyscale image stacks were put through the same grid method code. The only difference being, before processing of the greyscale image by the grid method, the synthetic grid images had random noise added (using Matlab's 'randn' function) to mimic the noise inherent to the experimental measurements. This noise was Gaussian, with a distribution scaled to have standard deviation equal to 0.45% of the dynamic range—determined from analysis of the experimental images. For more details on this procedure, please consult Fletcher *et al.* [37].

4. Results

Firstly, the FE displacement and acceleration fields of each model (rigid and compliant) are compared with the experimental measurements. Note that these relate to the front (visible) surface of the test specimen. Excess of 45 initial experimental runs were performed to optimize the experimental set up. A final set of five runs were performed with identical parameters. Of these five, one particular experimental run was selected for comparison with the two models. This was because it was the 'best' set of images for processing via the grid method; it contained the highest contrast between light and dark areas of the grid (best illumination properties). In addition, this run was representative: it showed fields repeated on four of the five final runs. The anomalous run (in the final set) was discarded as the front of the high-speed jet generated was incoherent. The region of interest for both the modelling output and synthetic grid images was selected to match that of the experiments.

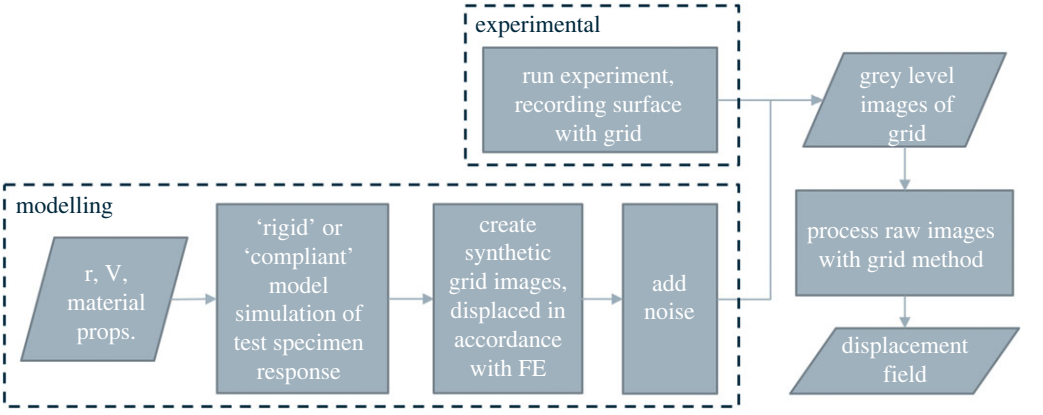

Figure 7. Image deformation simulations: process to enable effective comparison between experimental and modelling results.

The four comparative figures (figures 8–11) that follow have a consistent format:

— Three columns: the 'raw' FE data (either rigid or compliant); data from the synthetic grid images (constructed from the FE data) processed via the grid method; and the experimental recording, also processed using the grid method.
— Four rows, corresponding to four temporal positions: 1.0 µs, 1.6 µs, 2.2 µs and 2.8 µs. 1.0 µs was chosen as the first temporal position because it is the earliest point when displacement from the impingement is detectable in the experimental results. All four are following completion of the dynamic loading.
— Spatial coordinates, x and y, are as defined in figure 4.

Following the comparison between each model and the experimental measurements, the temporal variation of absorbed energy by the solid in the compliant model is shown.

(a) Rigid model versus experimental

Figure 8 shows the comparison between the displacement fields from the rigid model and those measured experimentally. The scale used for δ_y, ±2 µm is half that used for δ_x (±4 µm), hence the greater prominence of noise in the plots of δ_y. The simulated displacements, in both directions, are substantially less than that measured experimentally; it is barely visible when the scale is adjusted for the experimental measurements (as is the case here).

Figure 9 shows the comparison of the acceleration fields from the rigid model and the experimental measurements. Noise is more prominent in accelerations than displacements. However, the signal-to-noise ratio is sufficiently high that the acceleration resulting from the dynamic response of the material is visible in the experimental measurements. Unlike displacement (figure 8), the magnitudes of the features in the simulated fields of acceleration are similar to that measured experimentally. However, when synthetic images are generated from these fields, noise added and processed with the grid method, these features are barely visible (as shown in the middle column). This is caused by the very high spatial frequencies of the signal that cannot be reproduced by the limited spatial resolution of the camera. Interestingly, by just comparing the left and right columns, without the help of the synthetically deformed images, one would be tempted to accept the data as validation as qualitatively, the amplitudes match and the spatial features 'look similar'. This would lead to a false positive.

(b) Compliant model versus experimental

Figure 10 compares the displacement fields from the compliant model with the experimental measurements. As time increases, the displacement both simulated and measured on the surface

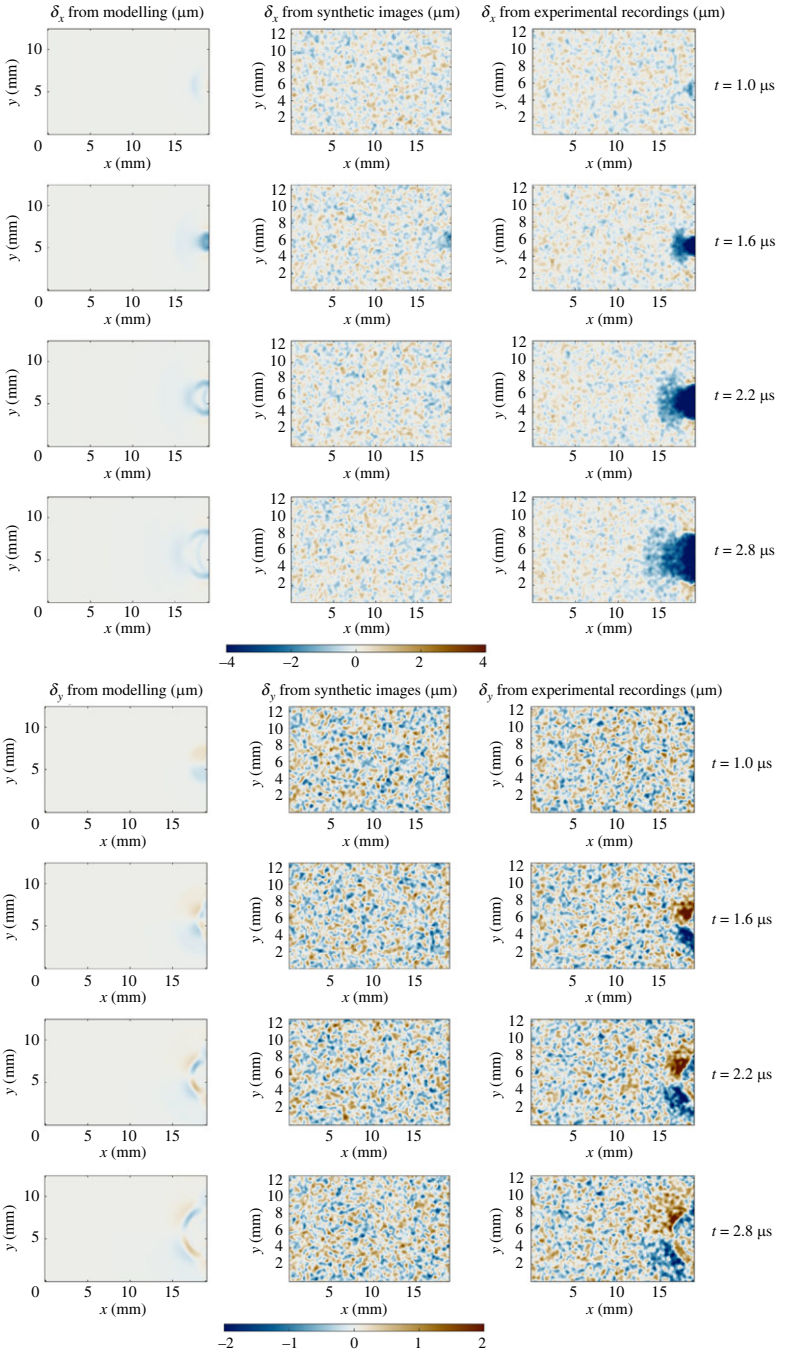

Figure 8. Fields of surface displacement, δ, in both x and y directions, for the rigid model, synthetic images (generated from model) and experimental recordings. Fields presented at four temporal positions: 1.0 μs, 1.6 μs, 2.2 μs and 2.8 μs. Note the scale in the y-direction is half that of the x-direction, ± 2 μm as opposed to ± 4 μm.

propagates across the specimen, from the impingement occurring on the right edge of the test specimen. Unlike the rigid model, both the magnitudes and spatial dimensions of features in the fields of δ_x and δ_y are consistent between the synthetic images (produced from the compliant model simulations) and the experimental measurements. There is one major divergence, most

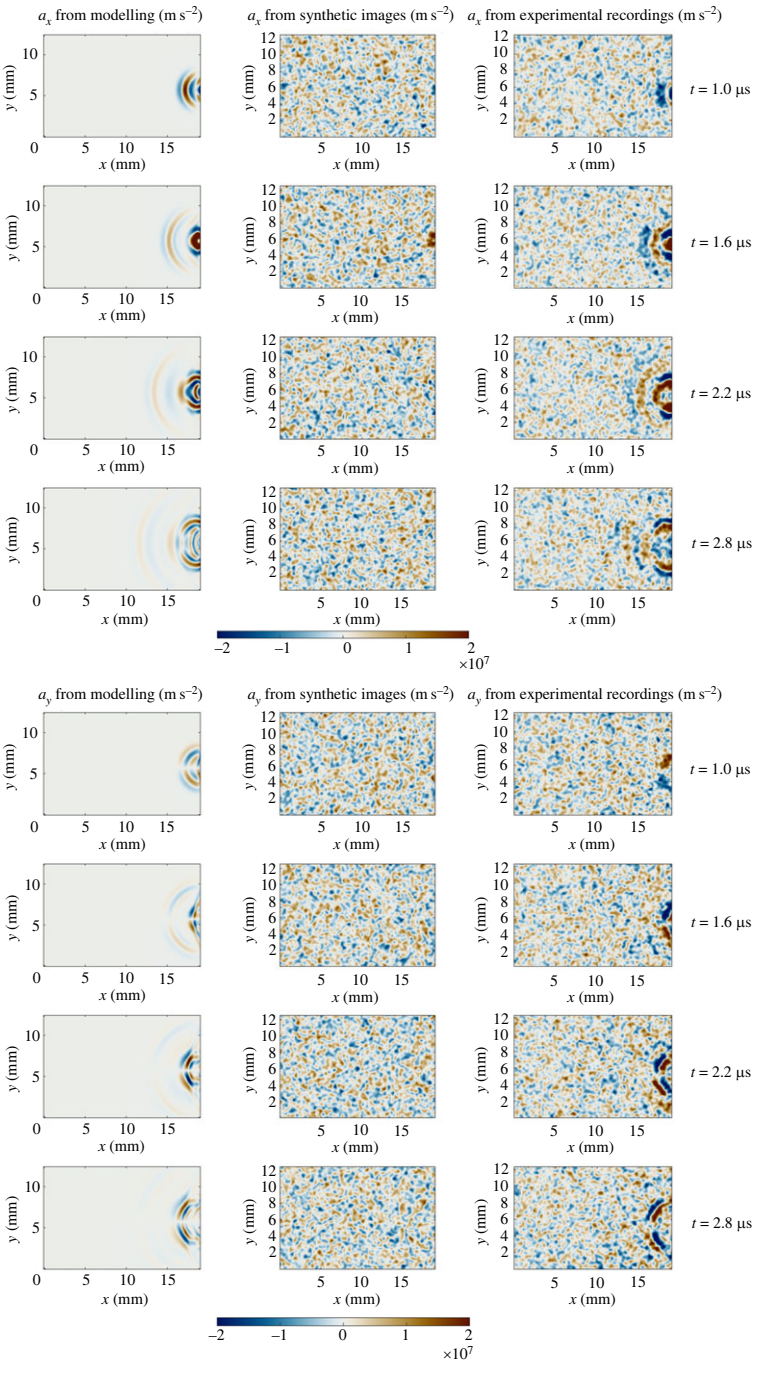

Figure 9. Fields of surface acceleration, a, in both x and y directions, for the rigid model, synthetic images (generated from model), and experimental recordings. Fields presented at four temporal positions: 1.0 µs, 1.6 µs, 2.2 µs and 2.8 µs. The scale of acceleration is ± two million g (approximately).

strongly visible in the plots of δ_x at 2.8 µs. The model shows a return to zero for δ_x behind the 'front' propagating across the surface. However, the experimental measurements show a continuation of negative displacement in the x-direction behind the front, at a similar magnitude to that of the front.

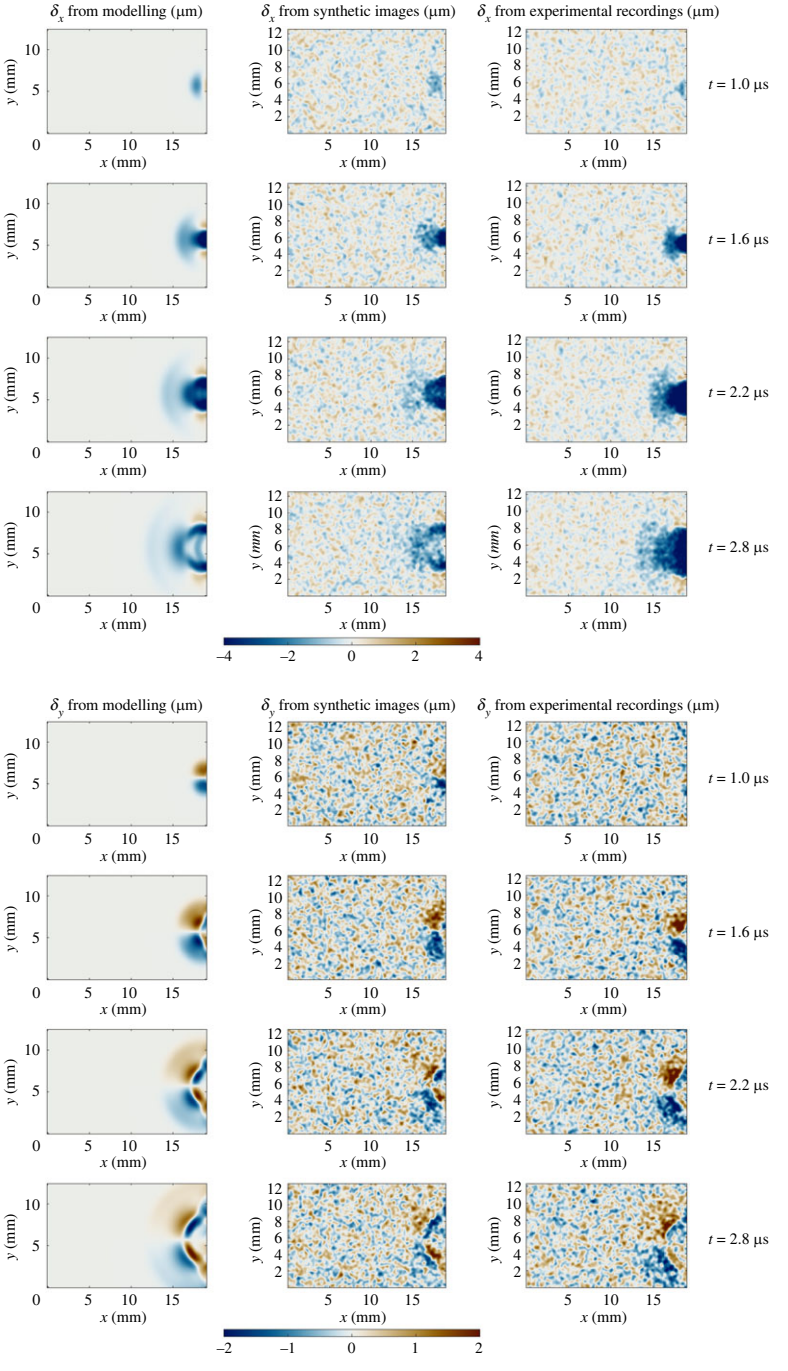

Figure 10. Fields of surface displacement, δ, in both x and y directions, for the compliant model, synthetic images (generated from model) and experimental recordings. Fields presented at four temporal positions: 1.0 μs, 1.6 μs, 2.2 μs and 2.8 μs. Note the scale in the y-direction is half that of the x-direction, ± 2 μm as opposed to ± 4 μm.

Figure 11 shows the comparison between the acceleration fields from the simulation and the experiment. As with displacement, the impingement occurring on the right leads to a propagation of the quantity, this time acceleration, across the specimen surface. The values and spatial frequencies in the fields of a_x and a_y are consistent between the synthetic images and the experimental measurements. The divergence observed in δ_x at 2.8 μs is not present in

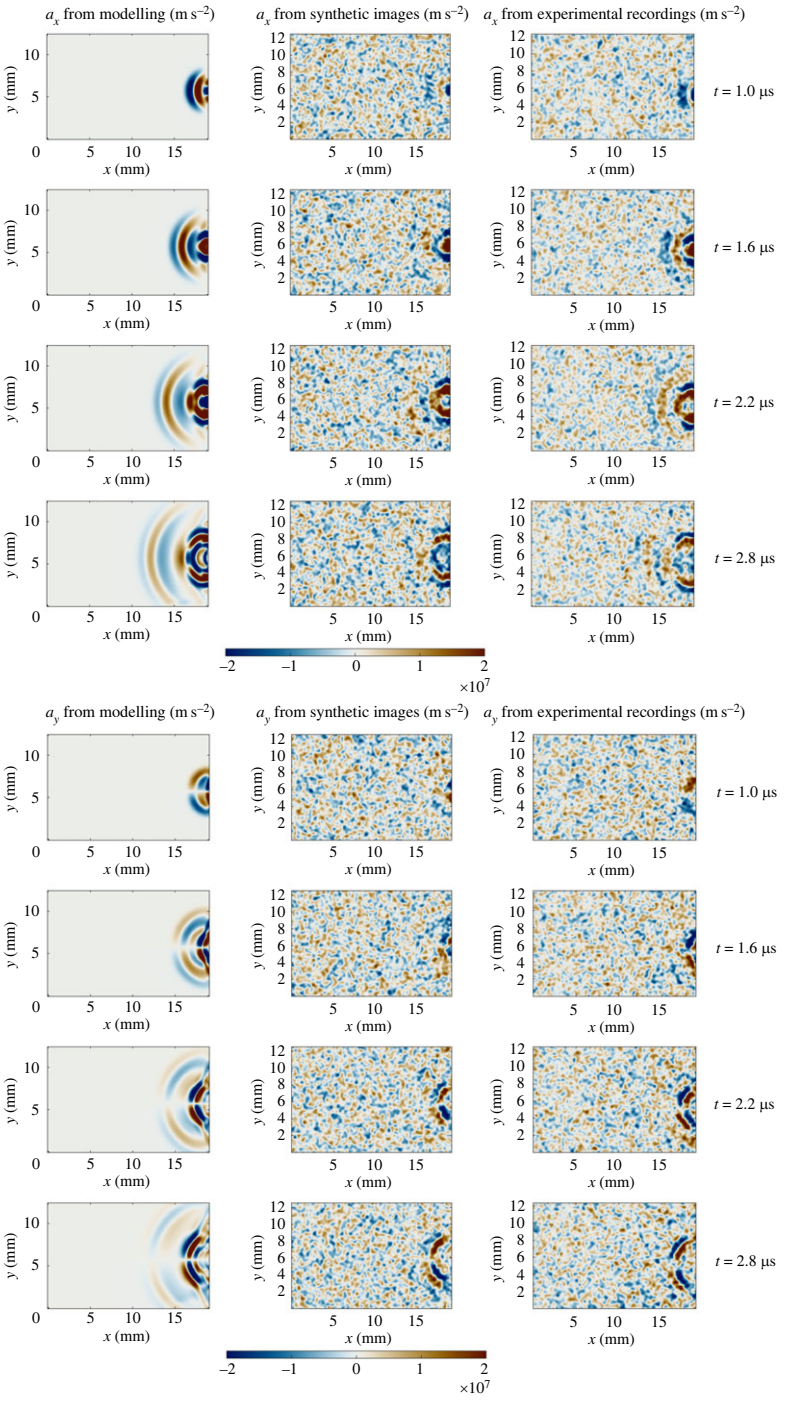

Figure 11. Fields of surface acceleration, a, in both x and y directions, for the compliant model, synthetic images (generated from model) and experimental recordings. Fields presented at four temporal positions: 1.0 µs, 1.6 µs, 2.2 µs and 2.8 µs. The scale of acceleration is ± two million g (approximately).

a_x at this time step, suggesting the additional displacement in the experimental results is not varying significantly with time (and generating significant temporal derivatives, e.g. velocity, acceleration).

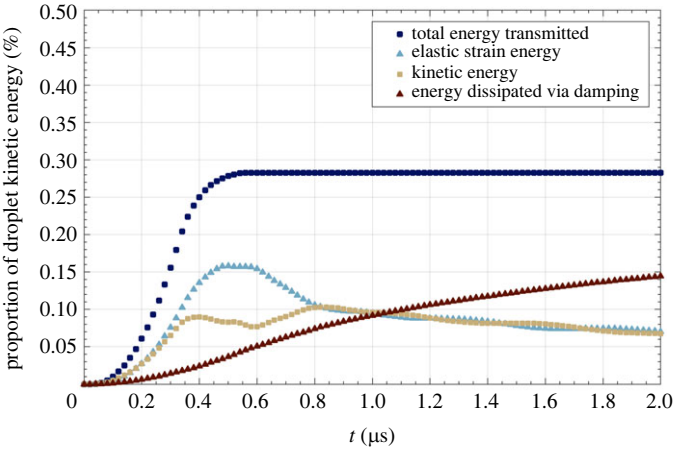

Figure 12. Temporal variation in total energy transmitted to solid material, expressed as a percentage of the kinetic energy of the impinging droplet. This comprises three components (also plotted): elastic strain energy, kinetic energy of solid, and the energy that has been dissipated by the small amount of beta damping.

(c) Energy transmitted by high-speed liquid impingement

Figure 12 shows the distribution of strain energy in the solid from the compliant simulation. There are three contributions: elastic strain energy, kinetic energy (of the solid) and the energy that have been dissipated by the small amount of beta damping. The magnitude of each has been expressed as a percentage of the kinetic energy of a droplet with a radius of 2.4 mm, impinging at 233 m s^{-1} (the same as the model inputs). During the period while the load is applied, up to 0.6 µs (approximately), the total energy transmitted increases to a maximum of just below 0.3% of the droplet's kinetic energy. During the loading period, the elastic strain energy and kinetic energy of the solid increase more rapidly that the energy dissipated by damping. However, following cessation of the load, these two contributions decrease gradually as a greater proportion of the total energy transmitted is dissipated by damping.

5. Discussion

When the data of each model and experimental recordings are compared, a clear difference is observed: those from the compliant model show a strong level of consistency with the measured fields of displacement and acceleration; the data from the rigid model do not. The implications of this main observation, along with other points, are discussed in the remainder of this section. We begin with how the results support current understanding, followed by how they challenge current thinking, and finally, limitations of this study are provided.

(a) Reinforcing current understanding

For the high-speed impingement that was created experimentally in this work, previous research would suggest that a high-pressure is initially applied on the specimen, over an area a fraction of the droplet size, which is rapidly released to pressures at least an order of magnitude lower. A typical response can be expected to occur within the specimen: the generation of compressive and shear bulk waves. These will all be very transient (have small wavelengths) and should, in the case of a semi-infinite half-space, propagate in an approximately hemispheric shape from the point of impingement. Analysis of the experimental full-field measurements on the test specimen surface supports this description of events. Firstly, there is a time delay before any displacement or acceleration is experienced on the specimen surface recorded. This is due to the time required for the waves to propagate from the point of impingement, half-way through-thickness, to the surface measured. Once visible on the specimen surface, the expected wave structure becomes

increasingly apparent in both the measured displacement and acceleration fields; we see the faster bulk wave, the longitudinal compressive wave and visible furthest left in the fields, closely followed by the shear bulk wave. The only major divergence between the compliant model and experimental measurements was in the fields of δ_x (figure 10), for the latter temporal positions shown. Analysis of the corresponding acceleration fields suggested the additional displacement present in the experimental measurements was not varying significantly with time. The models simulated only the initial transient high pressure; the pressure an order of magnitude lower following was not included (as it thought not to contribute to WDE). It is likely that this additional displacement is a result of stagnation pressure generated by the freestream of the jet following the initial impingement.

(b) Challenging current understanding

The most substantial challenge to current understanding regards the assumption of a rigid solid surface in models of high-speed liquid impingement. The rigid model did not successfully simulate the effect of the dynamic loading. However, a model that incorporated the effect of the compliance of the solid surface was much more successful in reproducing the measured fields of displacement and acceleration. The comparison of the rigid model predictions with the experimental measurements suggests it was the spatial size of the features that prevented visibility in the acceleration fields processed from the synthetic images. Put plainly: the duration of the load was too short. This is unsurprising when the temporal variation in force from each model (figure 6) is considered—the loading of the compliant model lasts approximately three times longer. Several decades ago, Field *et al.* [16] shared the results that were used to modify the point at which the release waves propagate from the contact periphery to the central axis, extending the duration of the dynamic loading in the compliant model. Yet the use of the Cook water-hammer pressure [8], which assumes the solid surface to be rigid, remains widespread. The analytical modelling described in the significant reviews over the years [11,17,52] has assumed a rigid solid surface. Seminal works such as the Bowden & Field [10] criteria for lateral outflow jetting and the prediction of edge pressures by Heymann [24], widely referenced and still used now, frequently assume a rigid solid surface. Even more recent numerical modelling [43], again widely-cited, assumed a rigid surface. In short, the assumption of a rigid solid surface is embedded in much of the analysis of high-speed liquid impingement that has been developed over the years.

A defence to the rigid assumption could be that PMMA is more compliant than many of the materials which experience WDE in-service. Thus, perhaps for these stiffer materials, a rigid assumption has greater validity. Unfortunately for the success of this argument, Field *et al.* [16] also demonstrated that the rigid prediction of point of lateral outflow jetting significantly underpredicts the radial position where jetting commences for surfaces that are far stiffer, with a Young's modulus comparable to many of the engineering alloys in question. For example, if the value of β_j (position of lateral outflow jetting) for phosphor bronze found by Field *et al.* [16] (11°) is used in the compliant model, instead of the value for PMMA (14°), the duration of the high-pressure loading is 0.42 µs for the impingement generated in this work. This is still double that suggested by the rigid model. Thus, it is proposed that the results shown here, while a slightly extreme case, demonstrate the need to incorporate the compliance of the solid surface into both the modelling and analysis of a high-speed liquid impingement.

The success of the compliant model in replicating the effect of the dynamic loading also supports the model inputs used. To define the impingement, an equivalent droplet radius, derived and identified in our previous work [13], and impingement velocity, again identified previously [13], were used. The equivalent droplet radius assumed that the form of the jets was better described by a rotated second-order polynomial than spherical cap. This, of itself, was not particularly novel; it has been observed previously that curved-fronted high-speed jets are not perfectly spherical at the front [25,32,33]. However, employing an edge-detection algorithm to fit a second-order polynomial to the jet front, then using equation (2.1) to relate the identified

coefficient of the second-order term to an 'equivalent' droplet radius, was a new approach. Its success in this study raises questions of the accuracy of considering the jet to be a blunt cylinder, where the diameter is dictated by the orifice it has been ejected from, as has been the case in previous work [25]. For the blunt cylinder, the loading duration is controlled by the time for release waves to propagate from the circumference of the circular contact face to the central axis. If this is applied to the work here, 0.15 µs would be the predicted loading duration—far less than the 0.6 µs (approx.) predicted by the compliant model. In defence of the previous work [25], the difference in the conditions for which this was used, impingement velocity of approximately 600 m s^{-1} with an orifice diameter of 3 mm (both significantly greater), may result in the blunt cylinder being a more appropriate assumption.

The final challenge to current understanding is regarding the applicability of droplet kinetic energy as an indicator of erosive potential. Some researchers have recently attempted to relate WDE measured or predicted to the kinetic energy of the impinging droplet [53,54]. Unfortunately, this has led to some questionable simplifications being made. For example, Zhao *et al.* [53] constructed a model where 100% of the droplet's kinetic energy is transferred to the solid. A thought-experiment suggests that this does not make physical sense. What would happen if all the kinetic energy were transmitted from the liquid? Following the impingement, the liquid would stop moving (with respect to the solid surface). In reality, quite the reverse occurs: the liquid jets at velocities in excess of the impingement and flows, with considerable kinetic energy, across the solid surface. Thus, it is not surprising the compliant model predicts only a small fraction (less than 0.3%) of the droplet's initial kinetic energy is actually transferred to the solid.

(c) Limitations

Despite the strong level of consistency between the compliant model predictions and experimental results, only one set of impingement conditions on one material have been compared. This is not sufficient evidence for the promotion of a model that can be applied across various impingement conditions and materials. However, neither does this mean these results can be easily ignored. The use of a rigid assumption for the solid surface is widespread and, based on the results of Field *et al.* [16] (implemented in the compliant model), inappropriate; the droplet mechanics are significantly influenced by the compliance of the solid surface, even when the solid is comparatively stiff.

A second limitation of this work pertains to the resolution of the experimental results. It has been suggested that cavitation occurs following the initial compressible stage, resulting from the superposition of release waves (emitted from the contact periphery) on the central axis [55]. However, the spatial and temporal resolution of the full-field measurements used here are likely to be too coarse to detect the effect of loading resulting from the asymmetric collapse of cavitation bubbles. This is also the case for the non-uniform pressure thought to develop on the surface (frequently assumed to be uniform—including in the models developed in this work): its effects occur on a temporal or spatial scale that is not likely to be visible in the measurements taken. For the non-uniform pressure, investigation is also undermined by the choice of material, more specifically its comparatively high level of compliance. As shown in Field *et al.* [21], the analysis of Lesser [42] suggests that non-uniformity of pressure is significantly reduced by the compliance of PMMA.

6. Conclusion

— Despite much previous analysis of high-speed liquid impingement assuming a rigid solid surface, a modelling approach which employed this assumption significantly underpredicted the duration of the dynamic load. When the loading duration and magnitude were adjusted for the compliance of the surface, utilizing the work of de Haller [46] and Field *et al.* [16], the model reproduced the experimentally measured response of the PMMA test specimen with much greater success.

— The full-field measurements, and further analysis using the compliant model, support the existing qualitative description of the dynamic loading resulting from a high-speed liquid impingement: a high-pressure is applied to the surface for a fraction of a microsecond, over a spatially small area in comparison to the droplet size, which is followed by a pressure at least an order of magnitude lower.
— The compliant model predicted less than 0.3% of the equivalent droplet's initial kinetic energy was transferred to the solid in the experimental tests.
— The success of the compliant model also supported the approach of identifying an 'equivalent' droplet diameter [13], used as an input to the model, from the fitting of a second-order polynomial to the form of high-speed jet front.
— Synthetic image deformation based on the previous works [50,51] was instrumental in providing meaningful comparison between FE and experimental datasets.

Full-field measurements and the compliant model provide a strong basis for further investigation of high-speed liquid impingement across a wider range of conditions and materials, which these authors would strongly encourage. Moreover, detailed uncertainty analysis and quantitative comparison between the modelled and measured fields would also be beneficial. In this work, the results have been interpreted with the goal of better understanding the dynamic loading generated by a high-speed liquid impingement. Yet, the full-field measurements made provide a very rich experimental dataset for those modelling the compressible behaviour of liquids to validate with.

Data accessibility. The datasets supporting this study are openly available from the University of Southampton repository at https://doi.org/10.5258/SOTON/D1436 [56].

Declaration of AI use. We have not used AI-assisted technologies in creating this article.

Authors' contributions. C.B.B.-T.: data curation, formal analysis, investigation, methodology, project administration, software, validation, visualization, writing—original draft and writing—review and editing; T.J.H.: investigation, resources, supervision and writing—review and editing; L.F.: conceptualization, data curation, formal analysis, investigation, methodology, software, validation, visualization and writing—review and editing; R.W.: conceptualization, resources, writing—review and editing; F.P.: conceptualization, formal analysis, funding acquisition, methodology, project administration, resources, validation and writing—review and editing; R.J.K.W.: conceptualization, funding acquisition, project administration, resources, supervision and writing—review and editing.

All authors gave final approval for publication and agreed to be held accountable for the work performed therein.

Conflict of interest declaration. We declare we have no competing interests.

Funding. This research was funded by the Engineering and Physical Sciences Research Council (EPSRC): PhD Studentship ref. 1685710 (C.B.B.-T.) and Established Career Fellowship ref. EP/L026910/1 (F.P.).

Acknowledgements. C.B.B.-T. would like to thank Dr Aleksander Marek, Dr Jared Van Blitterswyk and Dr Sam Parry for the helpful discussions regarding the investigation.

Disclaimer. The funders had no role in the design of the study; in the collection, analyses, or interpretation of data; in the writing of the manuscript; or in the decision to publish the results.

References

1. Lesser M. 1995 Thirty years of liquid impact research: a tutorial review. *Wear* **186–187**, 28–34. (doi:10.1016/0043-1648(95)07190-3)
2. Staniša B, Ivušić V. 1995 Erosion behaviour and mechanisms for steam turbine rotor blades. *Wear* **186–187**, 395–400. (doi:10.1016/0043-1648(95)07136-9)
3. Gohardani O. 2011 Impact of erosion testing aspects on current and future flight conditions. *Prog. Aerosp. Sci.* **47**, 280–303. (doi:10.1016/j.paerosci.2011.04.001)
4. Crockett HM, Horowitz JS. 2010 Erosion in nuclear piping systems. *J. Pressure Vessel Technol.* **132**, 024501. (doi:10.1115/1.4000509)
5. Slot HM, Gelinck ERM, Rentrop C, van der Heide E. 2015 Leading edge erosion of coated wind turbine blades: review of coating life models. *Renewable Energy* **80**, 837–848. (doi:10.1016/j.renene.2015.02.036)
6. Kamkar N, Bridier F, Bocher P, Jedrzejowski P. 2013 Water droplet erosion mechanisms in rolled Ti-6Al-4V. *Wear* **301**, 442–448. (doi:10.1016/j.wear.2013.01.005)

7. Sayma AI, Kim M. 2003 Leading-edge shape and aeroengine fan blade performance. *J. Propul. Power* **19**, 517–520. (doi:10.2514/2.6137)
8. Cook SS. 1928 Erosion by water-hammer. *Proc. R. Soc. Lond. A* **119**, 481–488. (doi:10.1098/rspa.1928.0107)
9. Adler WF. 1999 Rain impact retrospective and vision for the future. *Wear* **233**, 25–38. (doi:10.1016/S0043-1648(99)00191-X)
10. Bowden FP, Field JE. 1964 The brittle fracture of solids by liquid impact, by solid impact, and by shock. *Proc. R. Soc. Lond. A* **282**, 331–352. (doi:10.1098/rspa.1964.0236)
11. Field JE. 1999 ELSI conference: invited lecture. Liquid impact: theory, experiment, applications. *Wear* **233**, 1–12. (doi:10.1016/S0043-1648(99)00189-1)
12. Heymann FJ. 1992 Liquid impingement erosion. In *ASM Handbook, vol. 18: Friction, Lubrication, and Wear Technology* (ed. PJ Blau), section 11, pp. 221–231. Materials Park, OH: ASM International.
13. Burson-Thomas CB, Wellman R, Harvey TJ, Wood RJ. 2019 Water droplet erosion of aeroengine fan blades: the importance of form. *Wear* **426–427**, 507–517. (doi:10.1016/j.wear.2018.12.030)
14. Heymann FJ. 1968 On the shock wave velocity and impact pressure in high-speed liquid-solid impact. *J. Basic Eng.* **90**, 400–402. (doi:10.1115/1.3605114)
15. Bourne NK, Obara T, Field JE. 1997 High-speed photography and stress gauge studies of jet impact upon surfaces. *Phil. Trans. R. Soc. Lond. A* **355**, 607–623. (doi:10.1098/rsta.1997.0028)
16. Field JE, Dear JP, Ogren JE. 1989 The effects of target compliance on liquid drop impact. *J. Appl. Phys.* **65**, 533. (doi:10.1063/1.343136)
17. Adler WF. 1979 The mechanics of liquid impact. In *Treatise on materials science and technology* (ed. CM Preece), vol. 16, pp. 127–178. New York, NY: Academic Press.
18. Burson-Thomas CB, Wellman R, Harvey TJ, Wood RJK. 2018 Importance of surface curvature in modeling droplet impingement on fan blades. *J. Eng. Gas Turbines Power* **141**, 031005–031005–9. (doi:10.1115/1.4041149)
19. Rochester MC, Brunton JH. 1974 Surface pressure distribution during drop impingement. In *4th International Conference on Rain Erosion and Associated Phenomena* (eds AA Fyall, RB King), pp. 371–393. Farnborough, UK: RAE Farnborough.
20. Shi HH, Takayama K, Nagayasu N. 1995 The measurement of impact pressure and solid surface response in liquid-solid impact up to hypersonic range. *Wear* **186–187**, 352–359. (doi:10.1016/0043-1648(95)07141-5)
21. Field JE, Lesser MB, Dear JP. 1985 Studies of two-dimensional liquid-wedge impact and their relevance to liquid-drop impact problems. *Proc. R. Soc. Lond. A* **401**, 225–249. (doi:10.1098/rspa.1985.0096)
22. Dear JP, Field JE. 1988 High-speed photography of surface geometry effects in liquid/solid impact. *J. Appl. Phys.* **63**, 1015. (doi:10.1063/1.340000)
23. Hong YK, Moon KH. 2016 Experimental research on a waterjet to simulate erosion by impact of a water drop. *Wear* **368–369**, 116–123. (doi:10.1016/j.wear.2016.09.006)
24. Heymann FJ. 1969 High-speed impact between a liquid drop and a solid surface. *J. Appl. Phys.* **40**, 5113–5122. (doi:10.1063/1.1657361)
25. Bourne N. 2005 On impacting liquid jets and drops onto polymethylmethacrylate targets. *Proc. R. Soc. Lond. A* **461**, 1129–1145. (doi:10.1098/rspa.2004.1440)
26. Kondo T, Ando K. 2016 One-way-coupling simulation of cavitation accompanied by high-speed droplet impact. *Phys. Fluids* **28**, 033303. (doi:10.1063/1.4942894)
27. Adler WF, Hooker SV. 1978 Rain erosion behaviour of polymethylmethacrylate. *J. Mater. Sci.* **13**, 1015–1025. (doi:10.1007/BF00544696)
28. Field J, Walley S, Proud W, Goldrein H, Siviour C. 2004 Review of experimental techniques for high rate deformation and shock studies. *Int. J. Impact Eng.* **30**, 725–775. (doi:10.1016/j.ijimpeng.2004.03.005)
29. Grédiac M, Sur F, Blaysat B. 2016 The grid method for in-plane displacement and strain measurement: a review and analysis. *Strain* **52**, 205–243. (doi:10.1111/str.12182)
30. Bowden FP, Brunton JH. 1961 The deformation of solids by liquid impact at supersonic speeds. *Phil. Trans. R. Soc. Lond. A* **263**, 433–450. (doi:10.1098/rspa.1961.0172)
31. Lane WR. 1951 Shatter of drops in streams of air. *Industr. Eng. Chem.* **43**, 1312–1317. (doi:10.1021/ie50498a022)
32. Hand RJ, Field JE, Townsend D. 1991 The use of liquid jets to simulate angled drop impact. *J. Appl. Phys.* **70**, 7111–7118. (doi:10.1063/1.349793)

33. Field JE, Gorham D, Rickerby D. 1979 High-speed liquid jet and drop impact on brittle targets. In *Erosion: Prevention and Useful Applications, ASTM STP 664* (ed. WF Adler), pp. 298–319. Philadelphia, PA: American Society for Testing and Materials.
34. Trujillo-Pino A, Krissian K, Alemán-Flores M, Santana-Cedrés D. 2013 Accurate subpixel edge location based on partial area effect. *Image Vision Comput.* **31**, 72–90. (doi:10.1016/j.imavis.2012.10.005)
35. theplasticshop.co.uk. 2018 Perspex Cell Cast Acrylic; Technical Data Sheet. See https://www.theplasticshop.co.uk/plastic_technical_data_sheets/perspex_technical_properties_data_sheet.pdf (accessed: 27-9-2018).
36. Van Blitterswyk J, Fletcher L, Pierron F. 2018 Image-based inertial impact test for composite interlaminar tensile properties. *J. Dyn. Behav. Mater.* **4**, 543–572. (doi:10.1007/s40870-018-0175-1)
37. Fletcher L, Van Blitterswyk J, Pierron F. 2019 A manual for conducting image-based inertial impact (IBII) tests. See http://dx.doi.org/10.5258/SOTON/P0015.
38. Fletcher L, Van-Blitterswyk J, Pierron F. 2019 A novel image-based inertial impact test (IBII) for the transverse properties of composites at high strain rates. *J. Dyn. Behav. Mater.* **5**, 65–92. (doi:10.1007/s40870-019-00186-y)
39. Wu W, Liu Q, Wang B. 2021 Curved surface effect on high-speed droplet impingement. *J. Fluid Mech.* **909**, A7. (doi:10.1017/jfm.2020.926)
40. deBotton G. 1997 Modeling the impact of waterdrops on targets with a thin protective layer. *Comput. Model. Simul. Eng.* **2**, 177–194.
41. deBotton G. 1998 The interaction of a coated target and an impinging waterdrop. *Wear* **219**, 60–72. (doi:10.1016/S0043-1648(98)00226-9)
42. Lesser MB. 1981 Analytic solutions of liquid-drop impact problems. *Proc. R. Soc. Lond. A* **377**, 289–308. (doi:10.1098/rspa.1981.0125)
43. Haller KK, Ventikos Y, Poulikakos D, Monkewitz P. 2002 Computational study of high-speed liquid droplet impact. *J. Appl. Phys.* **92**, 2821–2828. (doi:10.1063/1.1495533)
44. Blowers RM. 1969 On the response of an elastic solid to droplet impact. *IMA J. Appl. Math. (Institute of Mathematics and Its Applications)* **5**, 167–193. (doi:10.1093/imamat/5.2.167)
45. Adler WF. 1977 Liquid drop collisions on deformable media. *J. Mater. Sci.* **12**, 1253–1271. (doi:10.1007/BF02426864)
46. de Haller P. 1933 Untersuchungen über die durch Kavitation hervorgerufenen Korrosionen. *Schweizerische Bauzeitung* **101**, **243**, 260.
47. Davis F, Pierron F. 2017 A novel method to characterize the impact response of PMMA. In *Annual SEM Conf. (Society for Experimental Mechanics), 12–15, June, Indianapolis, IN, USA*.
48. Jordan JL, Spowart JE, Kendall MJ, Woodworth B, Siviour CR. 2014 Mechanics of particulate composites with glassy polymer binders in compression. *Phil. Trans. R. Soc. A* **372**, 20130215. (doi:10.1098/rsta.2013.0215)
49. Pierron F, Zhu H, Siviour C. 2014 Beyond Hopkinson's bar. *Phil. Trans. R. Soc. A* **372**, 20130195. (doi:10.1098/rsta.2013.0195)
50. Rossi M, Pierron F. 2012 On the use of simulated experiments in designing tests for material characterization from full-field measurements. *Int. J. Solids Struct.* **49**, 420–435. (doi:10.1016/j.ijsolstr.2011.09.025)
51. Lava P, Jones EMC, Wittevrongel L, Pierron F. 2020 Validation of finite-element models using full-field experimental data: levelling finite-element analysis data through a digital image correlation engine. *Strain* **56**, e12350. (doi:10.1111/str.12350)
52. Engel OG. 1973 Damage produced by high-speed liquid-drop impacts. *J. Appl. Phys.* **44**, 692–704. (doi:10.1063/1.1662246)
53. Zhao J, Chen K, Liu R, Liang M. 2014 Modeling study of liquid impingement erosion of NiAl alloy. *Wear* **311**, 65–70. (doi:10.1016/j.wear.2014.01.003)
54. Kirols HS, Mahdipoor MS, Kevorkov D, Uihlein A, Medraj M. 2016 Energy based approach for understanding water droplet erosion. *Mater. Des.* **104**, 76–86. (doi:10.1016/j.matdes.2016.04.089)
55. Field JE, Camus JJ, Tinguely M, Obreschkow D, Farhat M. 2012 Cavitation in impacted drops and jets and the effect on erosion damage thresholds. *Wear* **290–291**, 154–160. (doi:10.1016/j.wear.2012.03.006)
56. Burson-Thomas C, Fletcher L, Pierron F. 2023 Raw images of ultra-high-speed videos to make full-field measurments. University of Southampton. (doi:10.5258/SOTON/D1436)